GFZ

Helmholtz-Zentrum
POTSDAM

Originally published as:

GJI Geomagnetism, rock magnetism and palaeomagnetism

A target-oriented magnetotelluric inversion approach for characterizing the low enthalpy Groß Schönebeck geothermal reservoir

G. Muñoz, O. Ritter and I. Moeck

Helmholtz Centre Potsdam, German Research Centre for Geosciences GFZ, Telegrafenberg, 14473 *Potsdam, Germany. E-mail: gmunoz@gfz-potsdam.de*

SUMMARY

Electrical conductivity is a key parameter for the exploration and characterization of geothermal reservoirs as hot mineralized formation water of active geothermal areas usually exhibits significantly higher conductivity than the surrounding host rock. Here we present results of a magnetotelluric (MT) exploration experiment carried out in the vicinity of the Groß Schönebeck geothermal test site in Northern Germany, where a doublet system of two 4.3-km deep boreholes was drilled to establish an *in situ* laboratory to investigate the potential for geothermal energy production. Classical 2-D smooth inversion of the MT data, recorded along two profiles, reveals a shallow conductive structure in good agreement with information from regional geology and seismic images. However, at the northernmost part of the profiles, the conductivity models reveal deep-reaching conductive structures, which appear uncorrelated with existing (geophysical or geological) data. Incorporating information from seismics as independent constraints for MT inversions allows us to examine the model space rigorously but target oriented. Employing so-called tear-zone inversions we can effectively derive an alternative class of models, which are consistent with the MT observations but also with the other data sets. We speculate that the zones of high conductivity imaged at reservoir depth are related areas of reduced thickness of the overlaying evaporite layer. The enhanced conductivity can be explained by a higher fracture density in anhydritic layers and/or generally lower resistivity of the pore fluid.

Key words: Electrical properties; Magnetotelluric.

INTRODUCTION

The Groß Schönebeck *in situ* geothermal laboratory, located 40 km north of Berlin in northeastern Germany, is a key site for testing the geothermal potential of deep sedimentary basins. The target reservoir is located in Lower Permian sandstones and volcanic strata, which host deep aquifers throughout the Northeast German Basin (NEGB, Huenges *et al.* 2007). The laboratory consists of two 4.3-km-deep boreholes. GrSk 3/90 was drilled in 1990 as a gas exploration well, later abandoned due to lack of productivity, and reopened in 2000 for geothermal exploration. The second well (GrSk 4/05) was drilled in 2006. Together, the two wells form a geothermal doublet system, with GrSk 4/05 being used for the extraction of thermal waters and GrSk 3/90 as the reinjection well. The NEGB setting is typical for deep sedimentary basins and for low-enthalpy reservoirs in general.

The electrical conductivity of the subsurface is known to be a very important parameter for characterizing geothermal systems. High-enthalpy (active) geothermal areas often exhibit high conductivity when compared with the surrounding non-geothermal environment. In such high-enthalpy geothermal reservoirs (e.g. Hengil in Iceland, Taupo Volcanic zone in New Zealand) the high-temperature cores

(*ca.* 300 °C) are typically imaged as low conductivity bodies overlain by a highly conductive cap layer. The high conductivity originates from alteration of clay minerals (Wright *et al.* 1985). In Groß Schönebeck, however, borehole cuttings and core logs have not detected any alteration of clay minerals. Instead, hot and mineralized (saline) fluids of the deep aquifers can be imaged as regions of high electrical conductivity.

To investigate the subsurface electrical conductivity structure for geothermal exploration purposes, electromagnetic (EM) and DC geo-electric geophysical methods are generally suitable (e.g. see Pellerin *et al.* 1996; Meju 2002 and references therein). If the geothermal target is located at depths of a few kilometres, however, as in the case for most middle- to low-enthalpy geothermal reservoirs, the only reliable method to reach such depths is magnetotellurics (MT).

In this paper we present the results of two MT profiles in the vicinity of the Groß Schönebeck geothermal test site. The goal of the experiments was to image the electrical conductivity structure of the area and delineating the location of possible reservoirs. The MT work is part of the I-GET project (Integrated Geophysical Exploration Techniques), funded by the European Union (EU), which aims at developing an innovative strategy for geophysical

exploration, integrating different techniques ranging from rock physics to seismics and MT. Existing seismic and well data suggested subhorizontal layering for the sediments of the Northeastern German Basin including the region of the Groß Schönebeck geothermal reservoir (Moeck *et al.* 2008). Such a layered, predominantly 1-D setting considerably reduces the information contained in the MT data and the inverse problem is reduced to fitting one complex element of the impedance tensor (see e.g. Ritter *et al*. 2005). In perfect 1-D conditions adjacent sites produce identical MT data. In practice this means only the product of conductivity and thicknesses of layers (their conductance) can be resolved. If the conductivity structure varies laterally the impedance tensor separates into so-called TE (transverse electric) and TM (transverse magnetic) modes, a vertical magnetic field component arises, and the data between neighbouring sites vary considerably.

In this paper we demonstrate that relatively small lateral deviations within the sedimentary layering can be resolved and modelled with MT if the data are sampled with sufficiently dense site spacing. Highly conductive materials at surface are typical for the NEGB. The presence of such a high conductivity layer causes a screening effect, which limits the resolution of MT at depth. In such cases it can be crucial to obtain independent information to constrain the inversion models. Due to operational problems with the logging tools, unfortunately there are no resistivity logs available from the Groß Schonebeck wells to calibrate the MT models but seismic and other well data can be used to derive a different class of models. To test the significance of structural details, we study the sensitivity, resolution and equivalences of the derived 2-D inversion models. The sections show a consistent resistivity distribution for the upper 4 km and two different model classes for the deeper parts. These two model classes fit the data equally well for the data quality obtained. As an additional step, we introduce a target-oriented tearzones inversion (incorporating *a priori* information from seismic and geological models) to produce resistivity models, which can be interpreted more consistently with respect to existing data. However, the MT models also reveal structures that cannot be found with other methods. These localized regions of high electrical conductivity at 4–5 km depth could be interesting targets for future drilling and thus provide important information for a characterization of other potential geothermal reservoirs in the Groß Schönebeck area.

Geological setting

The NEGB evolved as one of four sub-basins of the extensive South Permian Basin (SPB) system which reached from Central England to Poland (Ziegler 1990). The NEGB is faulted by NW–SE striking major faults and NE–NNE striking minor faults (Baltrusch & Klarner 1993). During this initial basin development, intermediate volcanic deposits covered parts of the basin floor. Sedimentary red beds of Lower Permian age (Rotliegend) cover the volcanic rocks and are restricted to fluvial depositional centres along the southern and eastern flank of the South Permian Basin whereas the basin centre is dominated by evapouritic sequences (Plein 1995) (Fig. 1a). Consequently, potential geothermal reservoirs are primarily attributed to the Lower Permian red beds as they are sufficiently porous to hold significant volumes of geothermal fluids (approximately 15 per cent porosity according to core logs, Moeck *et al.* 2008). In the Groß Schönebeck area the lower Permian red beds are overlain by 1200 m thick Upper Permian evapouritic successions, which include a mixture of shales, carbonates, anhydrite and salt rock and influence the structure of the Mesozoic and Cainozoic

overburden by its mobility and evolved ridges, diapirs and salt lows (Figs 1b and c and 2). Mesozoic and Cenozoic terrestrial and marine sediments cover these salt sequences.

Magnetotelluric data acquisition and processing

Magnetotelluric data were collected in two field experiments, in 2006 June–July, along a 40-km-long main profile centred on the well doublet (profile 1) and in 2007 February–March along a 20-km-parallel profile (profile 2) located 3 km further to the east (Fig. 2). For profile 1 a total of 55 MT stations were recorded with an average site spacing of 400 m in the central part of the profile; towards both ends of the profile the site spacing increased to 800 m. Profile 2 consists of 18 MT stations with an average spacing of 1 km. This configuration was chosen to obtain a high-resolution model in the vicinity of the boreholes and to get some controls on the background or regional resistivity distribution. At all sites the two horizontal components of the electric field and the three components of the magnetic field were measured in a period range from 0.001 s to 1000 s, using the S.P.A.M. MkIII (Ritter *et al*. 1998) and CASTLE systems of the Geophysical Instrument Pool Potsdam and Metronix induction coils. Given the amount of EM noise present in the survey area, a long recording time (6 d for the stations of profile 1 and 4 d for the stations of profile 2) was chosen to improve statistical properties during data processing. While working along profile 1, we collected data at an additional four remote reference stations, at distances between 70 and 130 km from the profile (see Fig. 2). None of these stations, however, showed satisfactory data quality. For profile 2, we recorded at a reference site near the Baltic Sea located 190 km away (Fig. 2), which gave much better results.

The data were processed using the robust processing algorithm described in Ritter *et al*. (1998) and Weckmann *et al*. (2005) and using the modifications of Krings (2007) for remote reference processing. For comparison, the data were also processed using the algorithm of Egbert (1997), which provided very similar results, indicating that the responses are robust with respect to the processing scheme. For profile 1, all four remote stations were tested as a reference with the most suitable one being chosen on a site-by-site basis. In general, the transfer function curves are smooth and reliable at periods shorter than 3 s, but at longer periods (including the so-called dead band, 1–10 s) the influence of EM noise is higher and some data points had to be discarded due to poor data quality. However, using remote reference processing was vital as a single site processing of the impedance tensor produced highly scattered and/or biased curves, especially at periods between 1 s and 100 s. The consistency between the apparent resistivity and phase curves was tested using the D+ algorithm to make sure that they are not affected by near-field effects produced by noise. Fig. 3 shows examples of apparent resistivity and phase curves from both profiles. Most of the curves show similar apparent resistivity values of roughly 40 Ωm at the highest frequencies, indicating that static shift is generally a minor problem. A few curves with higher static shift were manually moved to the common apparent resistivity level. The apparent resistivity curves vary similarly along both profiles, that is, at high frequencies both components have moderate values of approximately 40 Ωm and with increasing period apparent resistivities reach minimum values of approximately 1 Ωm until the curves split for periods longer than 10 s.

Fig. 4 shows a map of induction vectors at periods of 3 s, 30 s and 300 s in the Wiese convention in which they point away
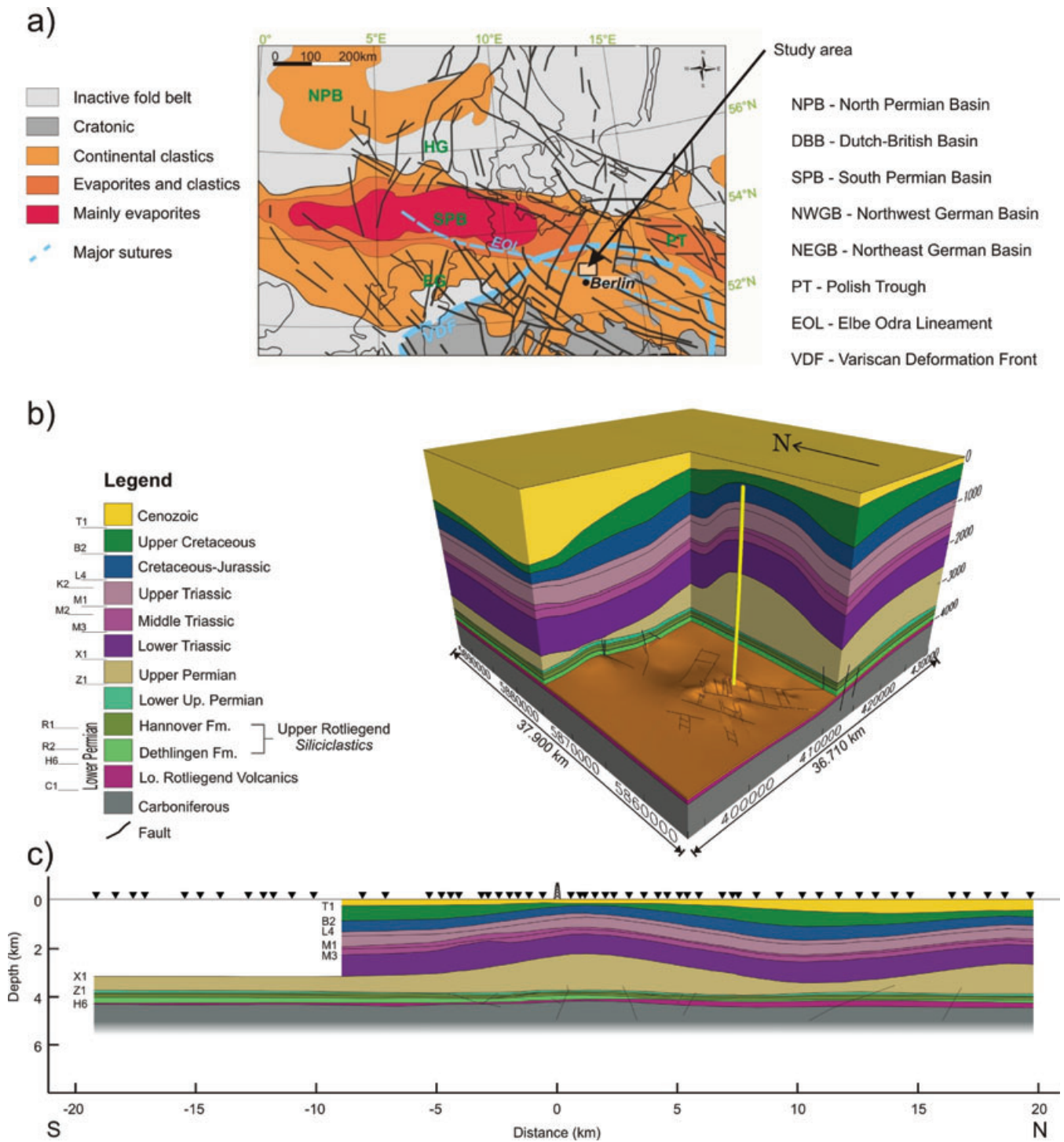
Figure 1. (a) Regional geological map of the South Permian Basin. (b) 3-D view of the geological model of the study area obtained from refraction seismic lines and regional borehole data (Moeck *et al.* 2008). (c) Cross-cut of the geological model along the main MT profile (profile 1). The geothermal test site is located in the Northeast German Basin. The potential geothermal reservoir is found in the Rotliegend —Lower Permian sedimentary red beds and underlying volcanic rock, below thick (>1000 m) evaporitic layers of the Upper Permian (represented by the thin green and purple layers between horizons H6 and Z1). Inverted triangles show the locations of the MT stations along profile 1.

from regions of high conductivity. At 3 s (and shorter periods) the induction vectors are small and scattered, as expected for a mostly 1-D character of the shallow subsurface. At 30 s, the induction vectors are slightly larger and show a reversal close to the location of the well doublet (marked with a blue star in the figure). South of

the borehole, the induction vectors point to the SW and north of it they are oriented southwards with a trend to the East. At 300 s, the arrows point consistently to the south along both profiles, probably reflecting a regional-scale structure. Generally, the induction vectors vary very consistently between sites and over period, which
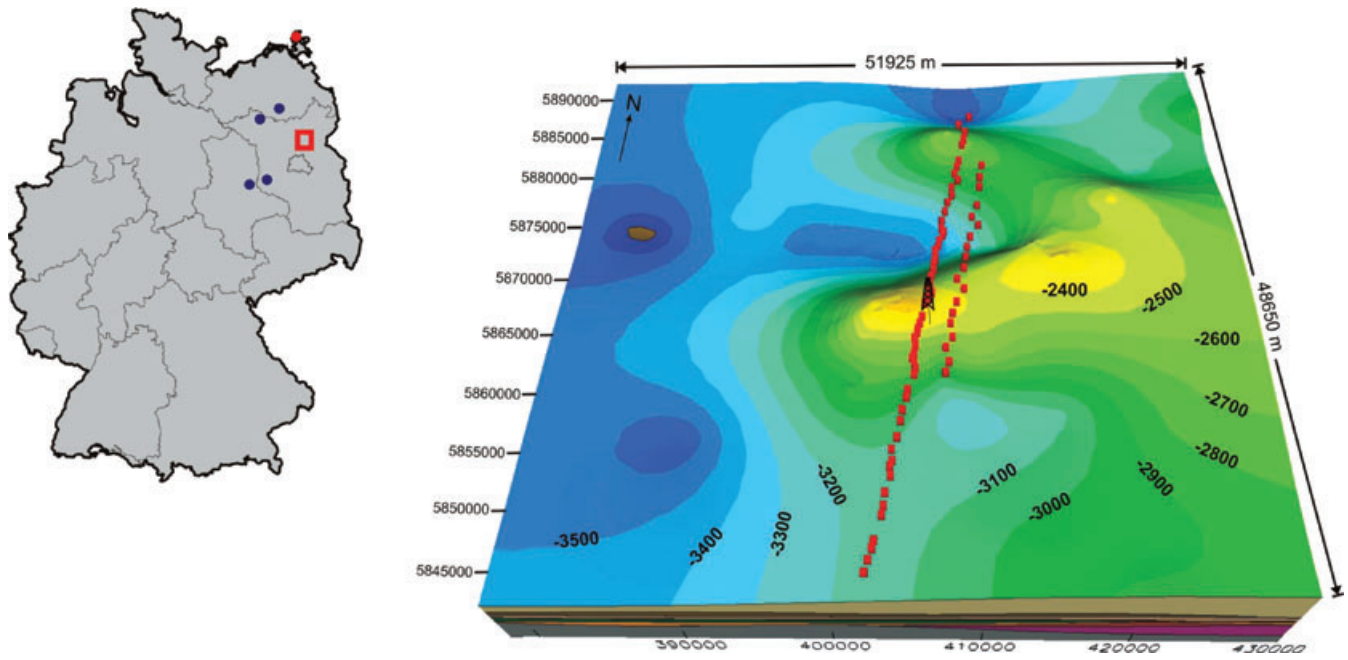
Figure 2. Location of the MT stations (red dots) on a map of the top of the Zechstein (evapouritic) formation (X1 in Fig. 1) from the 3-D geological model of Moeck *et al.* (2008). MT data were collected along a 40-km-long main profile (profile 1, 55 stations) centred on the well doublet and along a 20-km-parallel profile (profile 2, 18 stations) located 3 km further to the east. The red square on the map of Germany on the left-hand side shows the study area and the dots indicate the locations of the remote reference stations for the 2006 (blue) and 2007 (red) experiments.

confirms that noise is not dominating the observations but has been suppressed efficiently by the data processing.

The dimensionality of the data was analysed with the algorithm of Becken & Burkhardt (2004). This technique analyses the impedance tensor in terms of the polarization of the telluric vectors (columns of the impedance tensor), which are in the general case elliptically polarized. If a coordinate system can be found where the ellipticities of both telluric vectors vanish (i.e. they are linearly polarized), the impedance tensor can be decomposed in a regional 2-D tensor and a real distortion matrix (see e.g. Groom & Bailey 1989). In practice this coordinate system is sought by minimizing the sum of squared ellipticites over a range of periods and sites with respect to a rotation angle.

Fig. 5 presents two rose diagrams showing the distribution of regional strike directions for both profiles for periods longer than 1 s. In the case of profile 1, it can be seen that the strike directions vary consistently around 15–20° (with an inherent 90° ambiguity) with small dispersion. The ellipticities are close to zero and the distortion angles are mostly constant in the considered period range for all sites, indicating that the data are consistent with a 2-D resistivity structure [see Becken & Burkhardt (2004) for details]. The multisite, multiperiod analysis yields a regional strike direction of N70°W for profile 1. In the case of profile 2, the strike directions present a slightly higher dispersion, but with a concentration around 10–20° (again, with the inherent 90° ambiguity). Small ellipticities and consistent distortion angles suggest that a 2-D interpretation is also justified for profile 2. The multisite, multiperiod analysis of the impedance tensor for profile 2 gives a regional strike direction of N73°W, very similar to that of profile 1. For frequencies higher than 1 Hz, the ellipticities and distortion angles are very small for all the sites of both profiles. However, for the high frequencies strike directions are mostly undetermined which can be expected for a predominantly 1-D resistivity structure.

2-D inversion results

According to the tensor decomposition analysis the data of profile 1 were rotated to −70° and those of profile 2 to −73°. The 90° ambiguity was solved using the induction vectors (Fig. 4). Subsequent modelling and inversion was carried out with the Winglink software package (www.geosystem.net) using the 2-D inversion algorithm of Rodi & Mackie (2001). This algorithm seeks to minimize a functional (or objective function) that defines how well a model can explain the data. The functional consists of two terms, one term representing the fit to the data, and a second term representing a regularization functional used for numerical stabilization of the inversion process. With the introduction of the stabilizing term (Tikhonov & Arsenin 1977) the regularized inversion produces a minimum structure model. In the algorithm of Rodi and Mackie the stabilizing functional is a simple, second-difference operator, which approximates the Laplacian if the grid is uniform. This approach produces smooth models, with gradual changes of resistivity from one cell to the other as strong resistivity contrasts are penalized by the regularization functional. The weight of each of these two terms in the minimized functional is controlled via a trade-off parameter (τ), which has to be chosen for each model. A standard procedure for estimating the optimal τ value is the so-called L-curve study. Several inversions with different τ values are run, and for each of those the root mean square (rms) misfit (first term of the functional) is plotted against the model roughness (second term); the optimal value for τ is found close to the corner-point of the L-curve (i.e. the value which minimises both terms at the same time). The L-curves for both profiles in Fig. 6 reveal an optimum value for the smoothing parameter at $\tau = 10$ and hence, $\tau = 10$ was chosen for inverting both profiles. For the L-curve study, both TE and TM modes of apparent resistivity and phases and real and imaginary part of the geomagnetic (or vertical magnetic field) transfer functions were used, in a
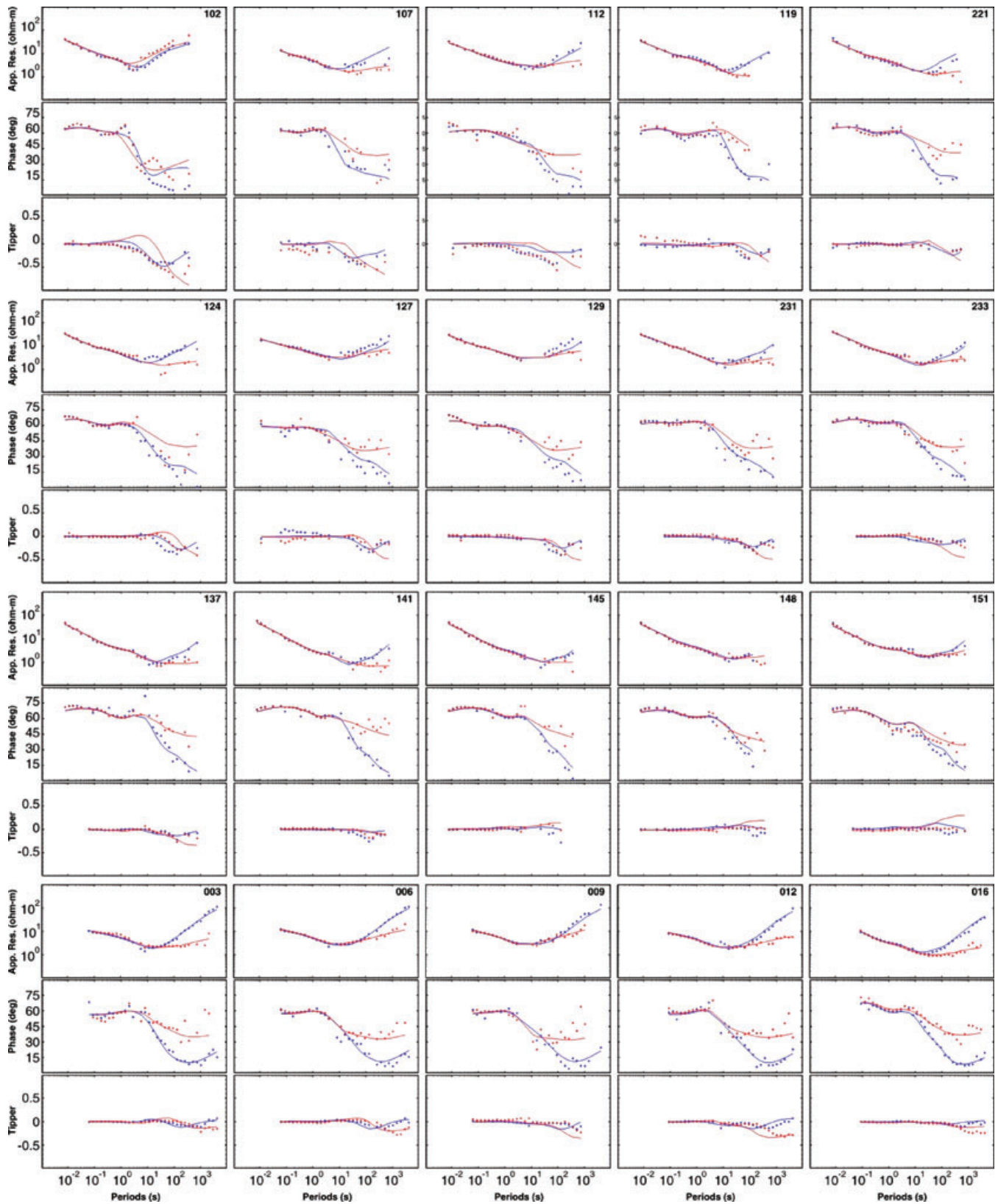
Figure 3. Examples of apparent resistivity, phase and vertical magnetic transfer function curves (period range 0.01 s to 1000 s) and 2-D modelling responses of the models in Fig. 8. The impedance tensor for profile 1 was rotated by $-70°$ and by $-73°$ for profile 2. Vertical magnetic transfer functions were projected accordingly to profile directions (see text and Fig. 5 for details on the tensor decomposition analysis and strike direction). For clarity data errors were omitted. For the inversion we set error floor levels of 10 per cent for resistivity, $1.5°$ for phases and 0.05 for vertical magnetic transfer functions.
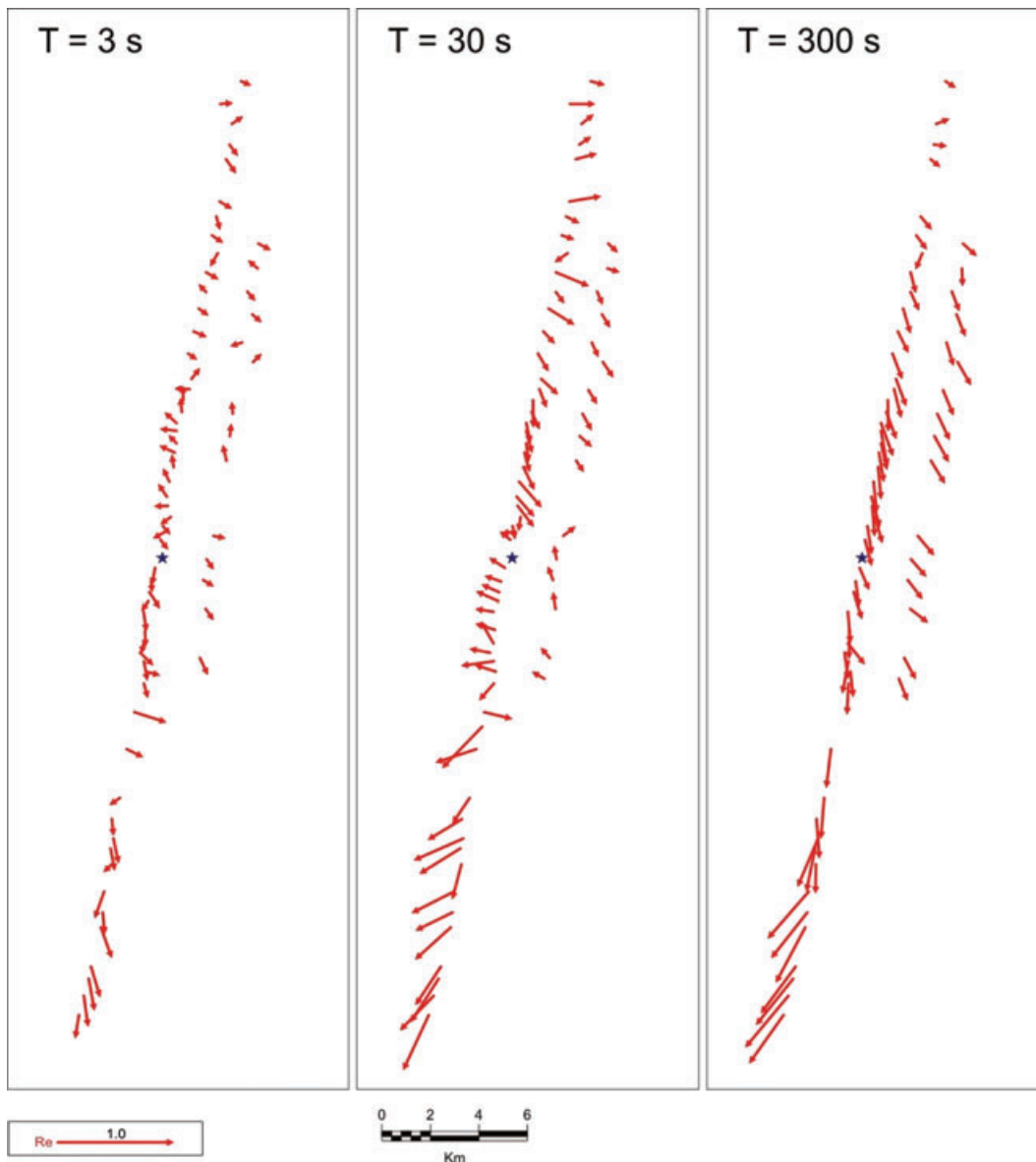
Figure 4. Induction arrows (Wiese convention) at 3 s, 30 s and 300 s for both MT profiles. The blue asterisk indicates the position of the well doublet. At shorter periods, the induction vectors are rather small and scattered. At longer periods, the vectors point consistently to the south, being larger in the southern half of the profiles, possibly indicating a regional structure.

wide frequency range from 10^{-3} to 10^3 Hz. Prior to the inversion the most obvious outliers in the data were rejected.

This type of study represents a first investigation of the model space, and helps to establish which features are stable for the various inversion runs. In Figs 7(a)–(d) we show results of 2-D inversions for profile 2 using different combinations of smoothing parameters and input data sets: model 7a was obtained using $\tau = 1$; model 7b was obtained with $\tau = 10$ but now by first inverting only the geomagnetic transfer functions and using the resulting model as the starting model for the joint inversion, the vertical magnetic transfer functions were given a higher weight in the inversion by setting a smaller error floor (0.025 in comparison with 0.05 for the other models); model 7c was obtained with $\tau = 100$. As can be seen, a conductive layer (C1-C2) appears in all models from the surface down to depths of approximately 2 km. Beneath this conductive layer, a region of high conductivity is found in the northern half of the profile (C3) and in some areas towards the centre or

southern end of the model (C4 in models 7a and 7d). However, the shape, location and conductivity of these anomalies change from model to model, that is, they are not uniquely determined by the data. Model 7d was obtained by inversion of TE and TM modes but excluding the geomagnetic transfer functions. It also shows the shallow conductive layer (C1-C2) and the (slightly) deeper conductive anomaly (C3). In addition, model 7d reveals a deeper conductive body (C4), which appears to be incompatible with the geomagnetic transfer function inversion result. The inclusion of the vertical magnetic field data pushes the northern conductive anomaly down and enlarges it (see Fig. 8b) while removing the deeper central conductive body. As expected, making use of the additional information contained in the vertical magnetic fields leads to a better constrained conductivity model. A similar result was found for profile 1, where a shallow conductive layer and two deeper conductive zones appeared as stable features throughout the inversion process.
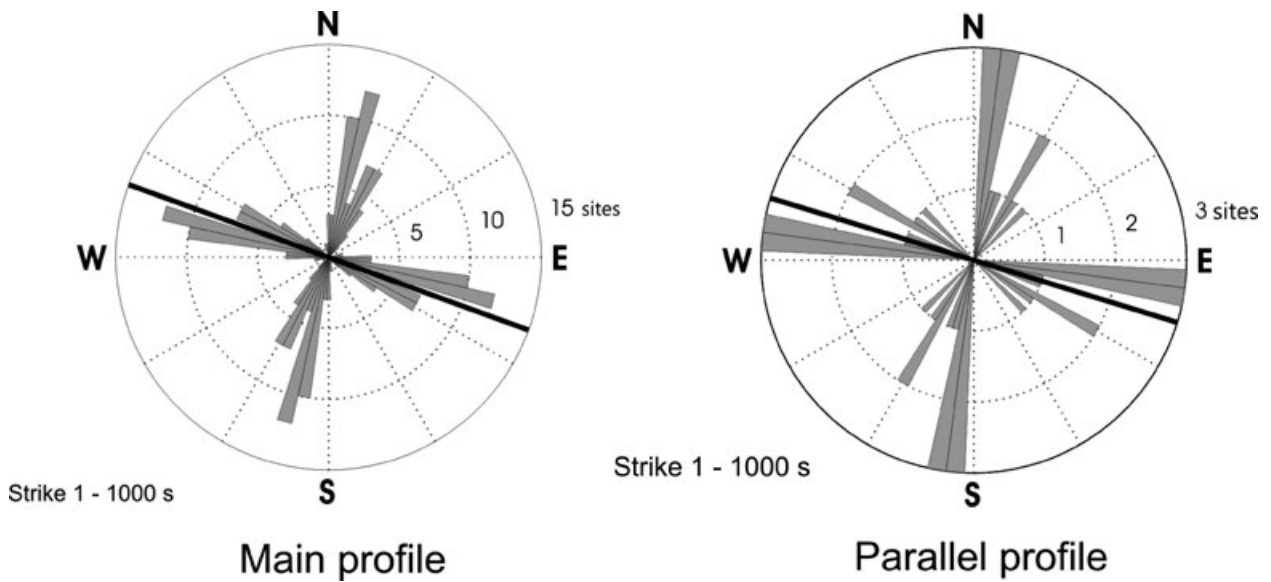
Figure 5. Rose diagrams of directional parameters for both profiles. The cumulative geoelectric strike directions obtained from impedance tensor analysis in the period range 1–1000 s cluster around 10–20° with an inherent 90° ambiguity for both profiles (with slightly higher dispersion for profile 2). The multisite, multi-period analysis yields regional strike directions of N70°W and N73°W, respectively (black solid lines on the diagrams).
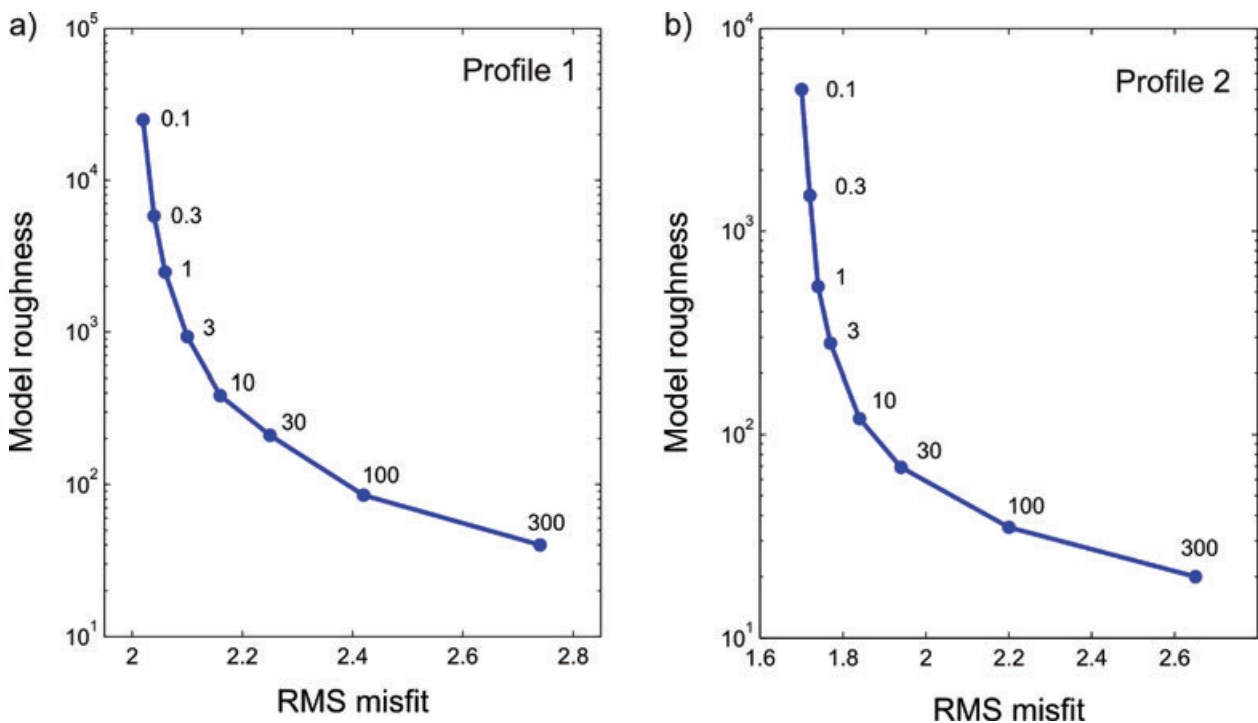

Figure 6. L-curve diagrams for both profiles. A set of six inversions was carried out for each profile with different values of the smoothness parameter τ (numbers above the dots). In both cases the corner point as a best compromise between data fit and model smoothness was found for $\tau = 10$. This value was then used for all subsequent inversions. Note that the model roughness is not comparable between the profiles because it also depends on the mesh discretization and number of parameters, which is different between the models.

Fig. 8(a) shows the smooth (or minimum structure) models obtained from the inversions of the apparent resistivity and phases of TE and TM modes as well as the vertical magnetic transfer functions using a regularization parameter of $\tau = 10$ (see above). The models are plotted together with sedimentary horizons from the geological model of Moeck *et al.* (2008) (see also Fig. 1). Using error floor settings of 10 per cent for the apparent resistivities, 1.5° for the phases and 0.05 for the geomagnetic transfer functions, rms misfits of 2.17

and 1.84 were obtained for profiles 1 and 2, respectively. The resistivity model for profile 1 (Fig. 8a) shows three shallow conductive bodies (C1, C3 and C4) which seem to form a continuous conductive layer extending from surface down to about 2.5 km depth with an antiform-like shape between sites 222 and 135. Towards the southern end of the profile another conductive body (C2) appears beneath the conductive layer, clearly disconnected from C1 and overlying a resistive body (R1) that extends from a depth of about 5 km towards
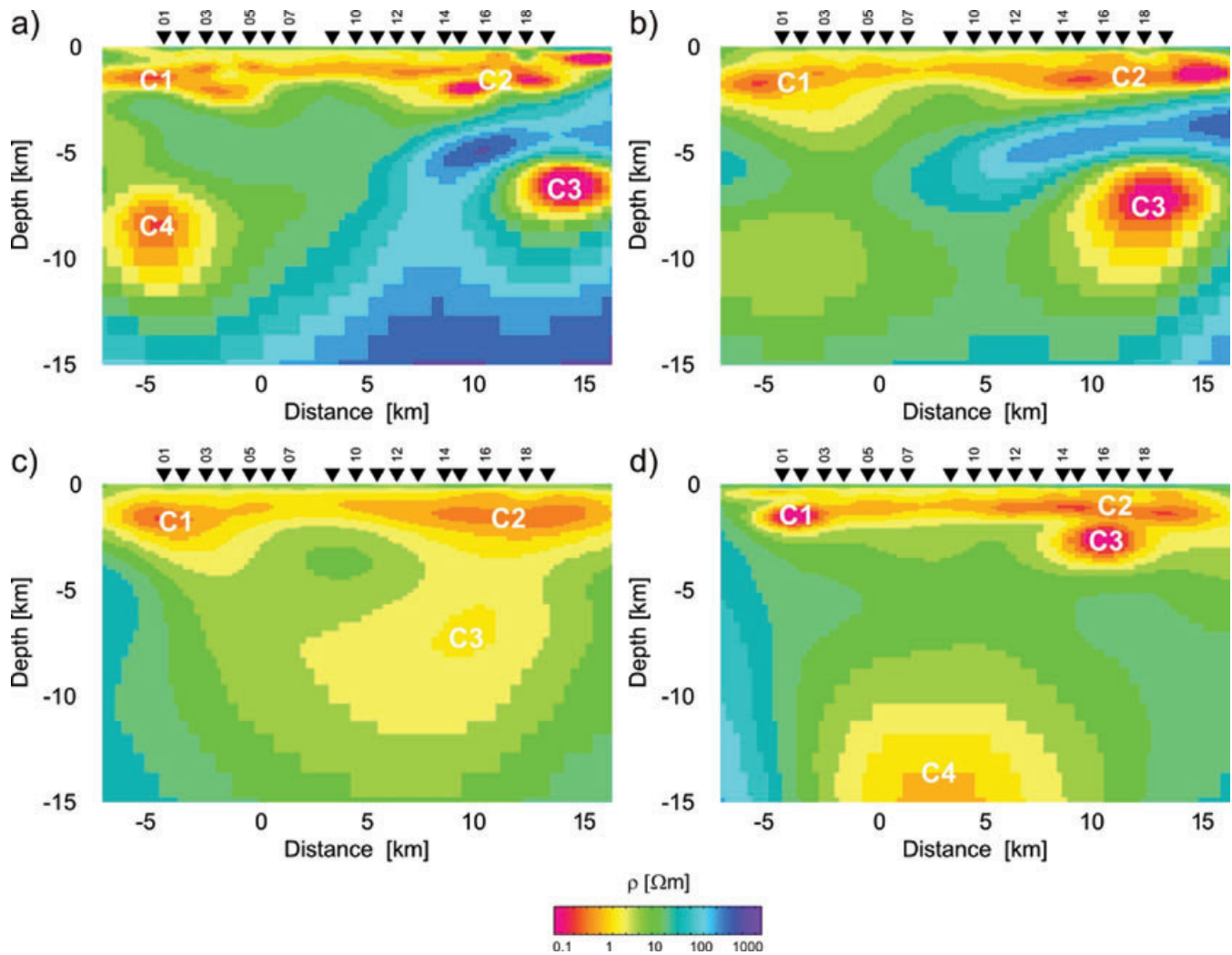
Figure 7. Model appraisal: resistivity models for profile 2 with different inversion parameters. In all cases (except for model b) a uniform half-space of 100 Ωm was used as starting model and the error floors were set to 10 per cent for apparent resistivity, 1.5° for the phases and 0.05 for the vertical magnetic transfer functions. Labels C denote prominent conductors. (a) Smooth inversion with $\tau = 1$. (b) Smooth inversion with $\tau = 10$ and error floor for the vertical magnetic transfer functions set as 0.025, the starting model was obtained from an inversion of vertical magnetic transfer functions only. (c) Smooth inversion with $\tau = 100$. (d) Smooth inversion of TE and TM modes only (vertical magnetic transfer functions were not included) with $\tau = 10$. In all models the upper 3 km exhibit a similar resistivity distribution (C1-C2) while deeper structures show greater variability.

the bottom of the model along the entire southern half of the profile. In contrast, a deep-reaching high conductivity body (C5) occupies most of the northern half of the model, from a depth of about 5 km downwards. The resistivity model obtained from profile 2 in Fig. 8(b) shows a very similar result with conductive bodies C1 and C2 forming a shallow conductive layer with antiform-like shape. The deep-reaching conductive body C3 is related in shape and location to C5 from profile 1 and a similar resistive body (R1) appears in the southernmost part of the model.

A striking feature of the resistivity models for both profiles 1 and 2 is the moderate resistivity associated with the Zechstein evaporites. Contrary to other salt structures in the NEGB that are usually imaged as high resistivity bodies with MT (e.g. Buehnemann *et al.* 2002), Fig. 8 shows a resistivity for the Zechstein evaporites comparable to that of the overlaying Lower Triassic sediments. The evaporites in the study area consist of a mixture of claystones (2.3 per cent), carbonates (1.3 per cent), anhydrite (6.6 per cent) and salt rock (89.8 per cent), as identified from borehole cuttings. Core logs and drill cuttings show interstratified

gypsum layers in the salt rock sections and salt-filled fractures in the brittle carbonates and anhydrites, indicating that brine circulation has occurred (Moeck *et al.* 2007). This hypothesis is also supported by results of seismic tomography (Bauer *et al.* 2010), which report salt pillows characterized by reduced velocities compared with the surroundings. The formation of these pillows was interpreted to be related to increased strain and fracturing caused by the tectonic deformation of the salt bodies (Popp & Kern 1998). Taking the composition and possible fracturing into account, the bulk resistivity of the lithologically heterogeneous Zechstein evaporites is lower than the values usually found in the literature for salt rocks.

Constrained inversions

The main MT profile is collocated with a seismic tomography profile (Bauer *et al.* 2010). The seismic velocity model shows consistently high Vp velocities >5.5 km s^{-1} for depths below 4 km, and a relatively homogeneous, layered velocity distribution. There are
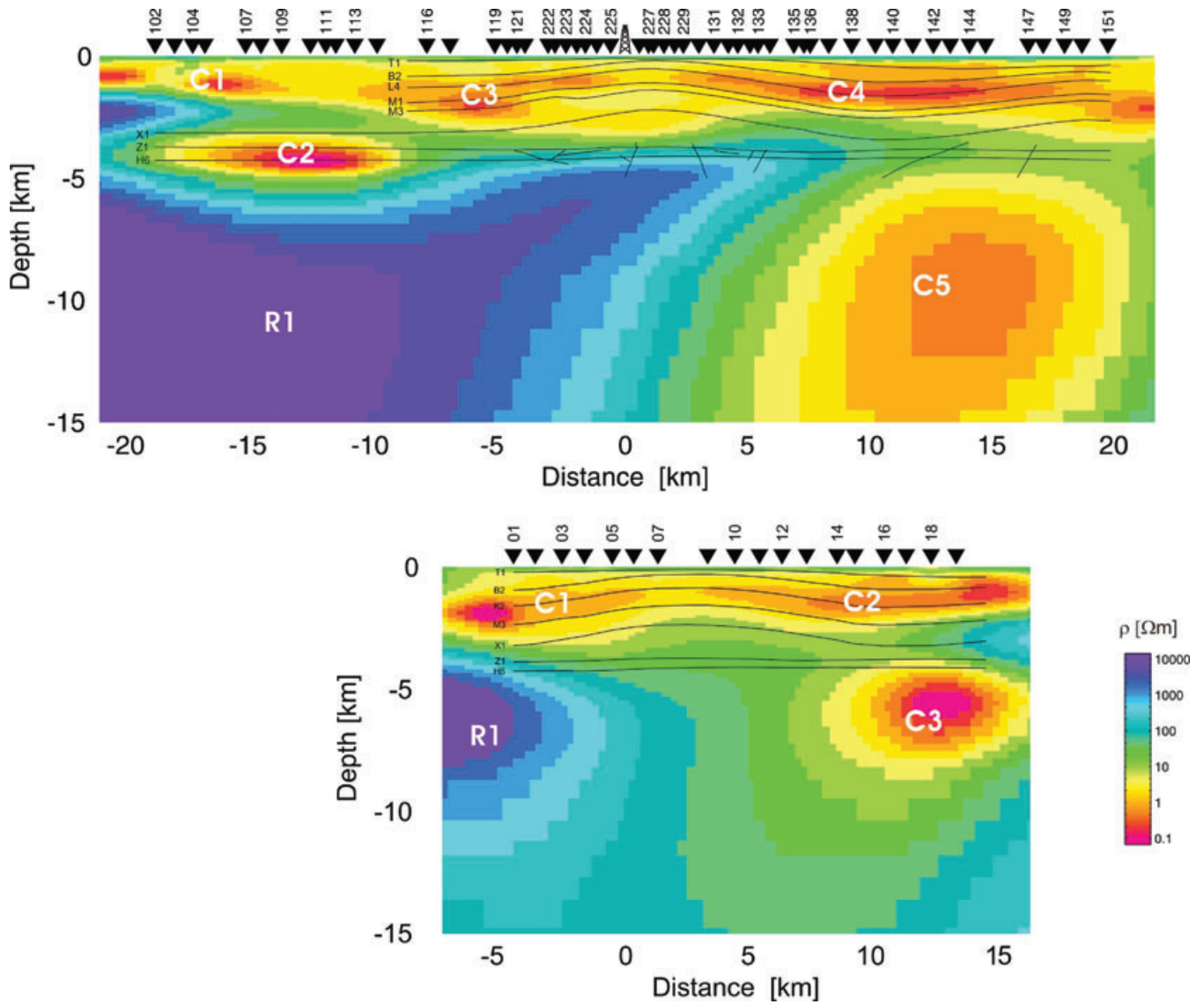
Figure 8. Resistivity models of both profiles obtained from smooth inversion. The thin black lines represent the stratigraphic horizons obtained from the geological model (Fig. 1). The models were obtained from the inversions of apparent resistivity and phases of TE and TM modes as well as the vertical magnetic transfer functions using a regularization parameter of $\tau = 10$; rms misfits of 2.17 and 1.84 were obtained for profiles 1 and 2, respectively (see text for details). C and R labels denote prominent conductive and resistive bodies; their significance is discussed in the text.

no indications in the Vp model, however, for features that could be related to the deep conductors C5 and C3 in profiles 1 and 2, respectively. In fact, the high Vp velocities at depth >4 km are among the best resolved parameters of the seismic models and they appear to be consistent with the borehole data, which indicate the basin floor at this depth. Furthermore, the pre-Permian basin floor in this region of the NEGB is represented by Lower Carboniferous Flysch facies, which is typically associated with high resistivity (Hoffmann *et al.* 2005).

To resolve this apparent mismatch between MT data and the other geo-information it must be tested if MT models exist which are compatible with a resistive basin floor at depths >4 km. To test this hypothesis a number of so-called tear-zones inversions were carried out. The inversion code of Rodi & Mackie (2001) allows dividing the model space into different regions, the tear zones; an application to MT data was described by Weckmann *et al.* (2007). In each of the regions the model norm is minimized independently

without interaction between model parameters belonging to different tear zones. This way, strong resistivity contrasts between tear zones are not penalized by the regularization of the inversion procedure. Tear-zones inversions result in a different class of models. In particular, they differ from the smooth inversion models, which are normally obtained. Smooth inversions can be regarded as an extreme class of models, as only models are sought that can explain the data with a minimum of structure. The tear-zones models, on the other hand, introduce a higher degree of subjectivity to the modelling process as the regions of tear zones are pre-defined by the modeller.

From the various smooth inversions runs we can conclude that the shallow conductive layers (C1-C3-C4 of profile 1 and C1-C2 of profile 2) are stable for a wide range of smoothing parameters and starting models, while the deeper conductive anomalies (C2 and C5 of profile 1 and C3 of profile 2) appear with a high degree of variability in position, size and resistivity values. It is the resolution

of these deep structures that we want to examine (and improve if possible).

For the starting models for the tear-zones inversions we divided the models into two tear zones based on the seismic horizon H6 (see Fig. 8), which is thought to represent the top of the Lower Permian volcanic rocks, and thus defines the basin floor. As starting model, we assigned a homogeneous resistivity of 100 Ωm to the zone above H6 and the region below H6 was substituted by a 1000 Ωm half-space, representing a resistive basin floor. In fact, in the smooth inversion models of Fig. 8 seismic horizon H6 coincides already with the top of the resistive body in the central part of profile 1 and the southern half of profile 2.

An inversion of apparent resistivity, phase and geomagnetic transfer functions was carried out for each profile, applying the same error floors as in the previous cases (10 per cent for the apparent resistivities, 1.5° for the phases and 0.05 for the geomagnetic transfer functions). The rms misfit of 2.27 for profile 1 and 1.85 for profile 2 are similar to the smooth inversion results. Fig. 9 shows the models obtained from the tear-zone inversions.

As expected, the upper 4 km of the models remain essentially the same for both types of inversion (compare Figs 8 and 9), that is, the general shape, position and conductivity of C1, C3 and C4 from profile 1 and of conductors C1 and C2 from profile 2 are similar. The strongest difference is found in the deeper part of the profiles, where the conductors C2-C5 and C3-C4 (see profiles 1 and 2 respectively) are now relocated above the resistive basement, showing much lower resistivity values (0.1 Ωm versus 1 Ωm) when compared with the smooth inversion models. However, the integrated
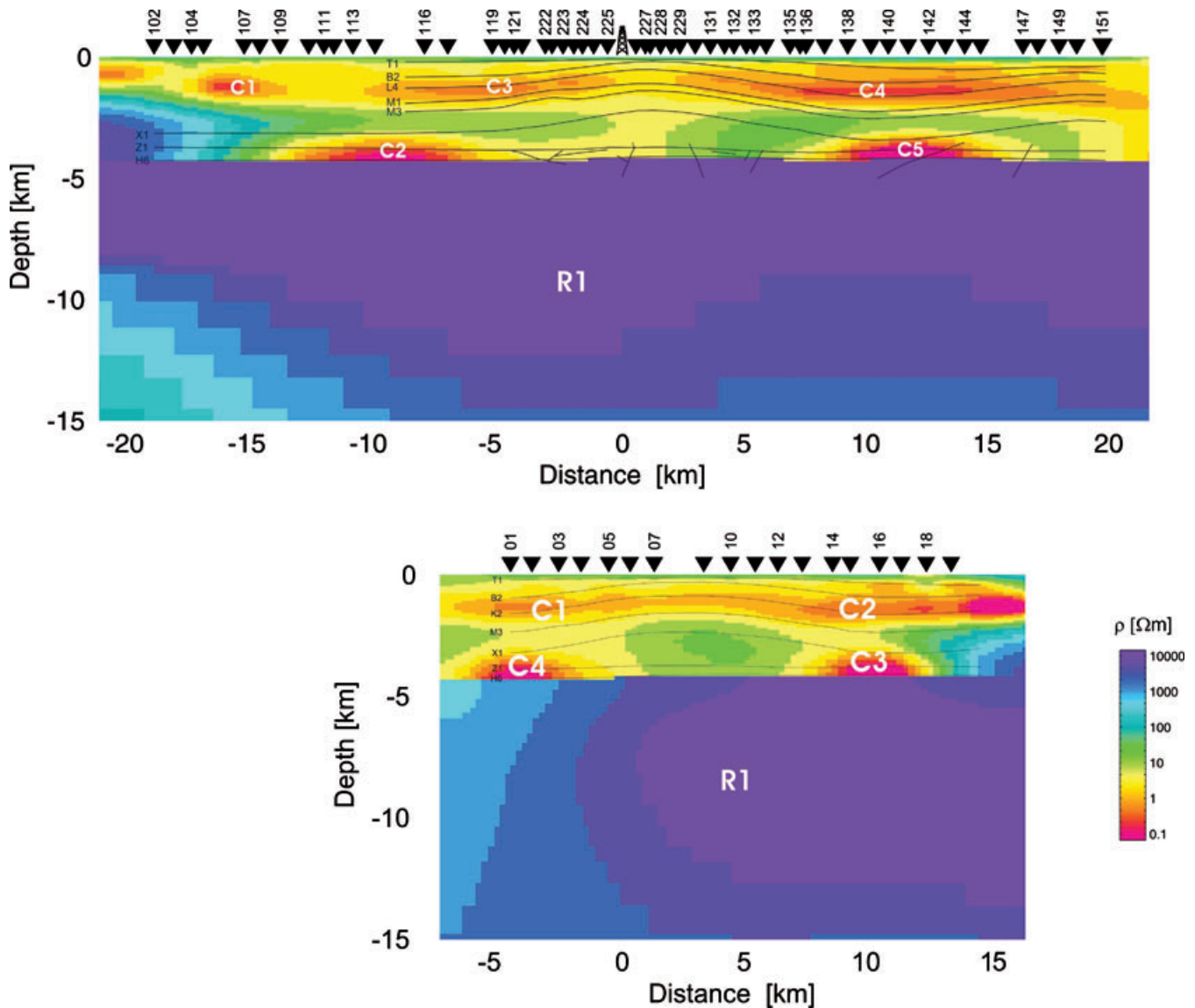
Figure 9. Resistivity models of both profiles obtained from tear-zones inversion. Horizon H6 divides the model into the two tear zones (see text for details). The thin black lines represent the stratigraphic horizons obtained from the geological model (Fig. 1). The models were obtained from the inversions of apparent resistivity and phases of TE and TM modes as well as the vertical magnetic transfer functions using a regularization parameter of $\tau = 10$; rms misfits of 2.27 and 1.85 were obtained for profiles 1 and 2, respectively (see text for details). C and R labels denote prominent conductive and resistive bodies; their significance is discussed in the text. The upper 4 km of the models are essentially the same as the models obtained from smooth inversion (Fig. 8). The deeper conductors below H6 (C5 and C2 in Fig. 8) are now located above the resistive basin floor (R1).

vertical conductance of anomalous body C5 is approximately 10 000 S for both models. The equivalence between the two models could be expected, as it corresponds to the classical conductance equivalence problem found in 1-D cases of a conductive layer sandwiched between two resistive layers.

An alternative way to test the compatibility of a high-resistivity basement with the data is to generate another class of models by investigating the parameter α that controls vertical to horizontal smoothing in the inversion code of Rodi & Mackie (2001). By setting a higher horizontal smoothing we can favour models, which show a larger lateral continuity of the conductivity structures and can present stronger resistivity contrast in the vertical direction. This type of inversion also implies a degree of subjectivity because it follows from the hypothesis that it is justified to penalize horizontal resistivity contrasts. Fig. 10 shows the result of the inversion of the data of profile 2 with $\tau = 10$ and $\alpha = 5$. The starting model for the inversion consists of a layered model with a resistivity of 100 Ωm from the surface down to a depth of 4.2 km and a 1000 Ωm half-space below, similar to the starting model for the tear-zones inversions. The resulting model is very similar to that obtained from tear-zones inversion (Fig. 9b), indicating that both approaches, tear-zones inversion and greater horizontal smoothing, provide a similar class of models.

Note that the overall rms misfit alone is not a significant criterion to determine if the two models are equivalent. However, after a close examination of the model responses of each site we conclude that both model classes are equivalent within the data errors. Additional information is therefore needed to establish a preference for one or the other.
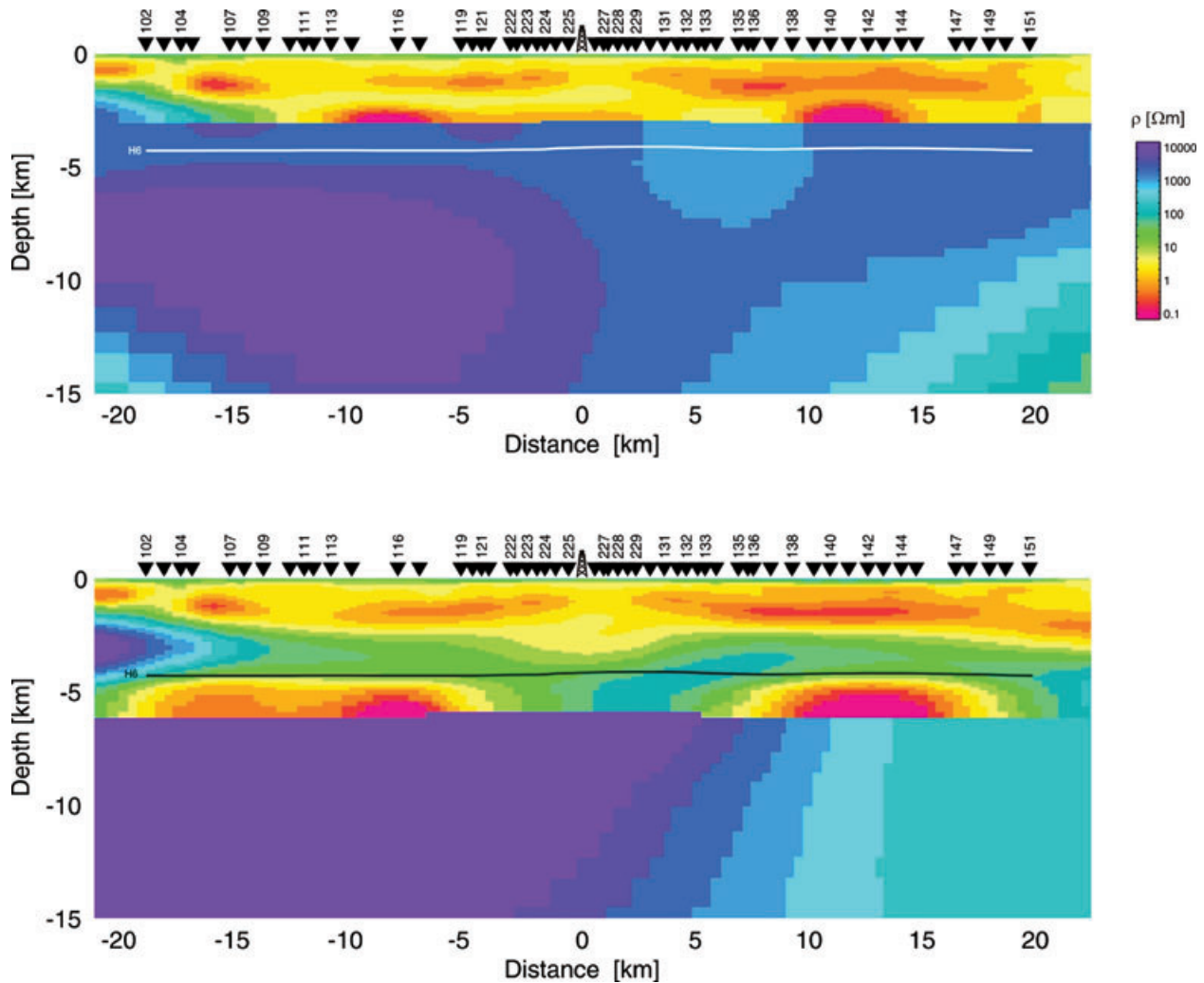
Sensitivity analysis

The sensitivity of the data with respect to structures was thoroughly tested by changing relevant parts of the models. Subsequently, we performed forward modelling studies and reinversion of the data using modified models as new starting models. For example, to test the sensitivity of the data to the depth of the basement we set tear-zone boundaries defining the basement 1 km shallower and 1 km deeper than in the original tear-zone inversion (i.e. when compared to the level of H6). The inversion models in Fig. 11 show that with a shallower basin floor of a tear zone 1 km above H6, the deep conductors (C5 and C3) merge with the shallow conductive layers (C1-C2-C4). As a consequence, the data fit gets considerably worse at the sites located above and near the anomalies. The model in Fig. 9 reached an rms of 1.78 for sites 138–151, while the rms increased to 2.46 for the model in Fig. 11(a). If we establish a resistive tear zone at greater depth a very similar model and data fit is obtained as with the tear zone at the H6 level. The tops of C2 and C5 for profile 1 and C3 and C4 for profile 2 appear at similar depths but the anomalies are thicker and slightly less conductive. Thus, we conclude that the resistive basin floor, if it exists, must be located at a minimum depth of 4.2 km (i.e. H6).

We ran a number of additional tear-zones inversions to analyse the sensitivity of the data to the deeper conductive anomalies. In a first stage, the starting models for these inversions were built by taking the upper part (above H6) from the smooth inversion model in Fig. 8(a) and by substituting the lower part (below H6) with a resistive half-space and conductive anomalies within the corresponding tear zone (see below). To avoid that the inversion was trapped in a
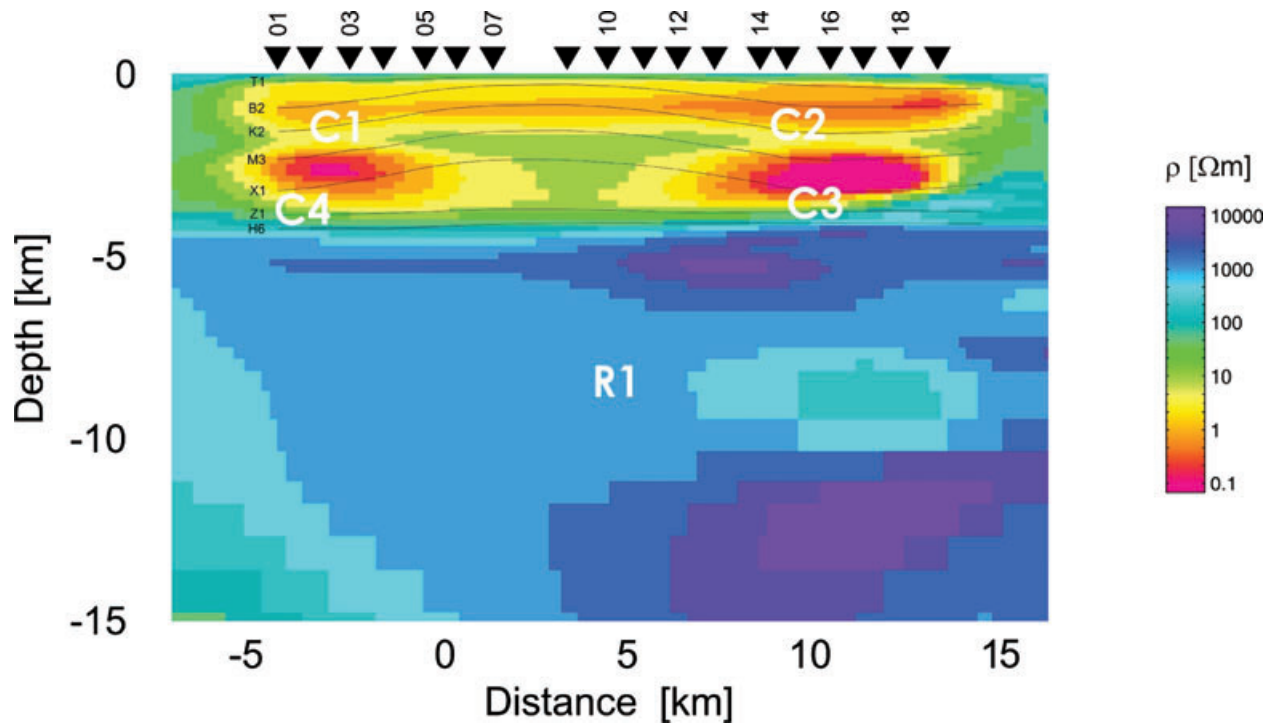
Figure 10. Resistivity model for profile 2 with enhanced horizontal smoothing. The starting model consists of a layered model with a resistivity of 100 Ωm from surface down to a depth of 4.2 km and a half-space of 1000 Ωm below. The smoothing parameters used for the inversion are $\tau = 10$ and $\alpha = 5$. The parameter α in the inversion code of Rodi & Mackie (2001) controls the ratio between horizontal and vertical smoothing. In this case a larger horizontal smoothing was preferred to obtain a stronger resistivity contrast corresponding with the basin floor. The model obtained shows resistivity structures consistent with those of the tear-zones inversion model (Fig. 9b).

Figure 11. Sensitivity analysis: comparison of two 2-D constrained inversion models with tear zone defining the resistive basin floor. In (a) the tear zone is placed 1 km above horizon H6 and in (b) 1 km below horizon H6. In case (a) the deeper conductors (C2 and C5) merge with the shallow conductive layer (C1-C3-C4) and the data misfit becomes significantly larger, indicating that the model is incompatible with the data. In case (b) the deeper conductors (C2 and C5) become thicker and the data misfit is very similar to that of the model in Fig. 9(a). Therefore, H6 indicates the minimum depth of the resistive basin floor (R1).

local minimum, we also substituted the upper half of the starting models with a homogenous 100 Ωm layer. The results showed that the tear-zone inversions are independent of the starting model as the shallow structures re-appeared as robust features.

Fig. 12 shows three models for profile 1 with different tear-zones setups. Model 12a features two tear zones, one in the area of conductor C2 and another in the area of C5. All starting models contained a resistive basement but not a tear zone at the level of H6. The models in Figs 12(b) and (c) are composed of similar tear zones in the areas of the deep conductors as in 12a albeit with different shapes and locations and a tear zone at the level of H6, comparable to the model in Fig. 9(a). In Fig. 12(c) the northern conductive anomaly is represented by two narrow vertical bodies located at the assumed positions of two deep-reaching faults, according to the geological model of Moeck *et al.* (2008) (see also Figs 8a and 9a). All three models show a similar overall rms misfit, comparable data misfits for individual sites in the northern part of the profile, also when compared to the unconstrained models in Figs 8 and 9. In all the inversions, however, a conductive body is found in the region below sites 140–147 at depths between 4 and

5 km. Forward modelling calculations confirm that these deeper conductive anomalies (C5) are required by the data. Therefore, we conclude that a conductive anomaly located below sites 138–147 exists at depth, but its geometry, exact position and size cannot be resolved unambiguously.

A remaining question is whether the deeper conductive anomalies (C5 and C2 in profiles 1 and 2, respectively) could be resolved with better data or if the lack of resolution is an inherent characteristic of the model. The upper 2–3 km of the resistivity models reveal layers of high conductivity material. Not unexpectedly this conductive layer has a shielding effect for the structures below. To investigate if better data quality and/or better station coverage would provide better resolution for deeper features, we computed forward responses of the smooth models in Fig. 8. After adding 3 per cent Gaussian noise to these synthetic data, they were taken as input for subsequent 2-D inversion tests. In addition, we added synthetic stations along the profile towards the north (stations 152–155). The results of the tear-zones inversion of these synthetic data are shown in Fig. 13. The inversion does reproduce a localized conductive anomaly above the basin floor, but also recovers an extended conductive body, similar
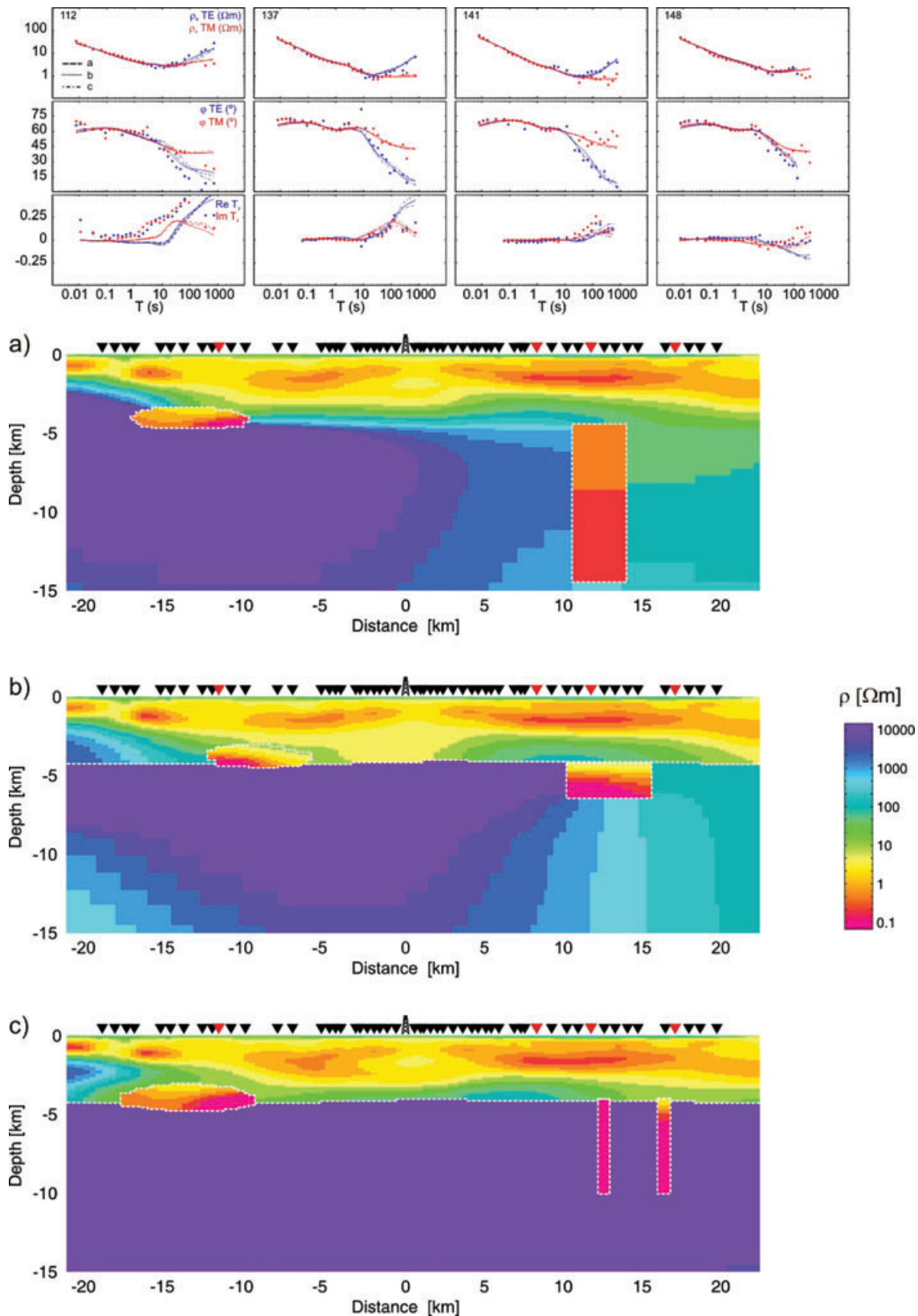
Figure 12. Sensitivity analysis: 2-D inversion models for profile 1 using different hypotheses for the deeper conductors C2 and C5 and different tear-zones configurations. The dashed white lines show the borders of the tear zones used for the different inversions. In model (a), the conductive anomaly C5 represents a deep-reaching subvertical body; no tear zone was included to define the basin floor. In model (b), the basin floor is defined by a tear zone and C5 by a broader and shorter anomaly with respect to model (a); in model (c), the deep conductive body C5 appears as split into two narrow and elongated structures (C5 and C6) at locations which coincide with two deep-reaching faults in the geological model of Moeck *et al.* (2008), see also Fig. 1. The upper panel compares the responses of the three resistivity models with those from the model in Fig. 9(a). Within the data accuracy, the model responses are indistinguishable.
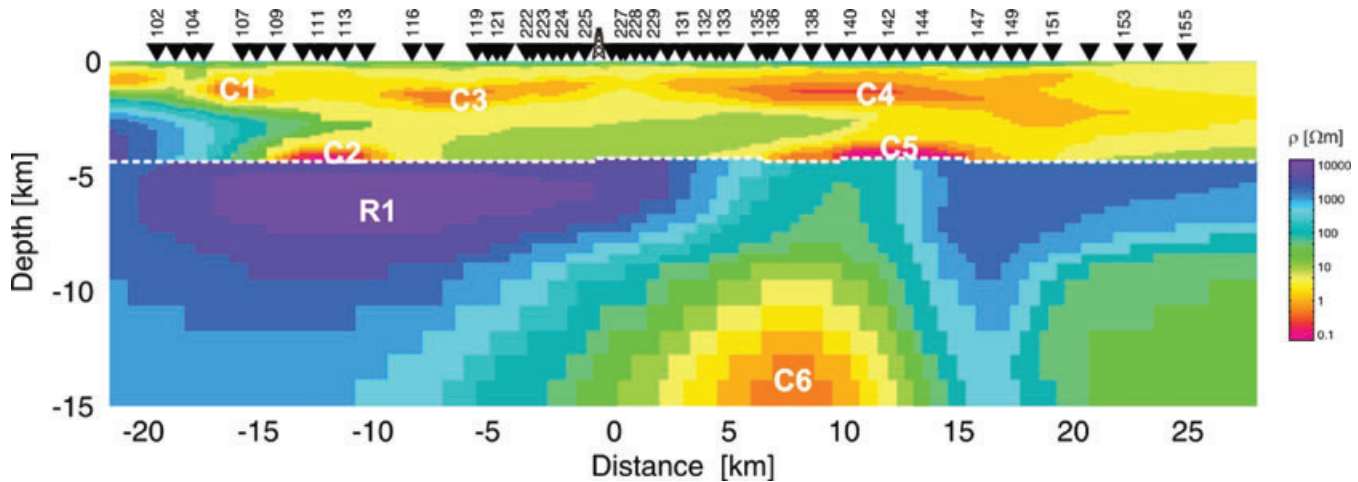
Figure 13. Resistivity section of profile 1 obtained using the forward responses of the model of Fig. 8(a) with 3 per cent Gaussian noise added as input data for the inversion. Additional synthetic stations (152–155) were included in the inversion to simulate a higher station density in the northern part of the profile. A tear zone was established below the level of horizon H6. The resistivity structure above the tear zone is very similar to that of the model in Fig. 9(a), but within the tear zone an additional, deeper conductive body (C6) appears. This extended anomaly is similar to C5 in the model of Fig. 8(a). Clearly, the synthetic data is incompatible with a model containing a resistive basement and a localized conductor above it (C5), like in the model of Fig. 9(a). The equivalence between the models of Figs 8 and 9 is not inherent to MT, but imposed by limited data quality.

to C5 in Fig. 8(a). This indicates that the equivalence between the model classes is not an inherent one, but depends on the quality of the data. Therefore, resistivity sections would be much better constrained by using high-quality data measured along a more extended profile.

Analysis of 3-D effects

An evapouritic layer of variable thickness with an updoming near the centre of the profiles as suggested by the geological model in Figs 1 and 2 could produce 3-D effects in the data. However, the dimensionality analysis of the MT data reveals very consistent strike directions for most of the stations along both profiles (Fig. 5). The similarity of the obtained resistivity models for both profiles also supports that a 2-D approach is suitable to explain the observed data. Given that the main source of a 3-D geometry would correspond to the updoming of the Zechstein evapourites we would expect only a small effect as we have already discussed that the resistivity values of the evapourites do not differ considerably from those of the overlaying sediments.

However, to test the influence of a finite strike of the resistivity structures more quantitatively, a 3-D forward analysis was carried out using the code of Mackie *et al*. (1993) included in the Winglink software package. Taking the resistivity models from Fig. 9 as a basis, a 3-D model was constructed using simplified resistivity structures. The model size was $75 \times 55 \times 20$ km with a mesh consisting of $91 \times 31 \times 24$ cells with an average size of 500×500 m in horizontal direction in the central part of the model and thicknesses of 50 m at the surface and increasing with depth. The stability of the mesh was tested by comparing the 3-D responses for a body of infinite length to 2-D responses derived using the code of Rodi & Mackie (2001) with the same mesh size. This test shows that the responses are not affected by numerical instabilities due to insufficient mesh size or conflict with the boundaries. The 3-D model includes the shallow conductive layer and the resistive basin floor. The resistivity of the Zechstein evapourites was assumed to be of similar value as the Lower Triassic sediments. The deep high conductivity anomalies associated with areas of reduced evapourite

thickness (see below) were discontinued approximately 6 km west of profile 1, according to the geometry of the evapouritic structures of the geological model (Fig. 2). Responses of this synthetic 3-D model were calculated for a range of periods between 0.001 and 1000 s.

Fig. 14 shows a view of the 3-D model and responses of some selected sites near the centre of the profiles together with the responses of the 2-D obtained from a slice of the 3-D model at the location of profile 1. The responses of the 3-D model are reasonably similar to those of the 2-D model, particularly in TE mode (the modes being defined according to the 2-D case). The TM phases show slightly larger difference, especially at long periods. These differences however are of the same magnitude as the average data misfit. Given the similarity between the 2-D and 3-D responses over the entire period range for all sites so that we can conclude that the 2-D approach taken is mostly appropriate even though some kind of 3-D influence cannot be ruled out altogether. A more complete 3-D approach using 3-D inversion would need more data west of profile 1 to better control the extension of the deep conductive anomalies and is beyond the realms of this paper.

Interpretation and discussion

For the interpretation we will focus on the models obtained with the 2-D tear-zones inversion (Fig. 9), which include a resistive basin floor compatible with the seismic tomography model. However, we should keep in mind that from the MT data alone we cannot rule out the possibility of an extended deep-reaching conductive body beneath the northern part of the profiles.

Comparison of the resistivity model in Fig. 9 with the geological model of Moeck *et al.* (2008) reveals a concert of structures. At surface, the Tertiary sediments are imaged as a moderately conductive layer (20–50 Ωm) in both profiles. These porous, unconsolidated sediments comprise sands, gravel and clay. The shallow conductive layers (C1–C3–C4 of profile 1 and C1–C2 of profile 2) present an antiform shape and coincide with the Mesozoic sedimentary sequences above the Buntsandstein (M3). This sequence encompasses weak or soft rocks such as clay, marl, marly limestone and some thin
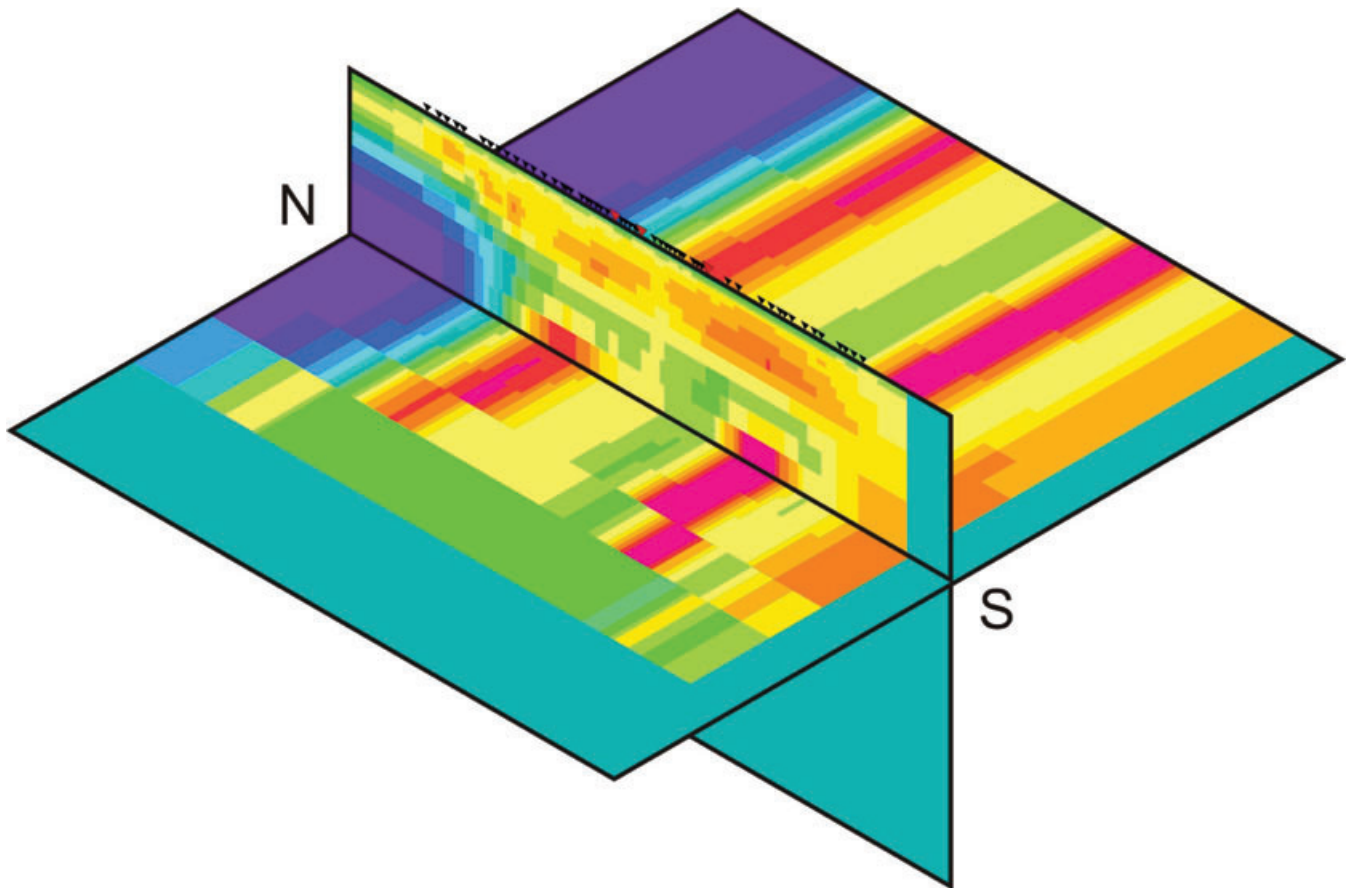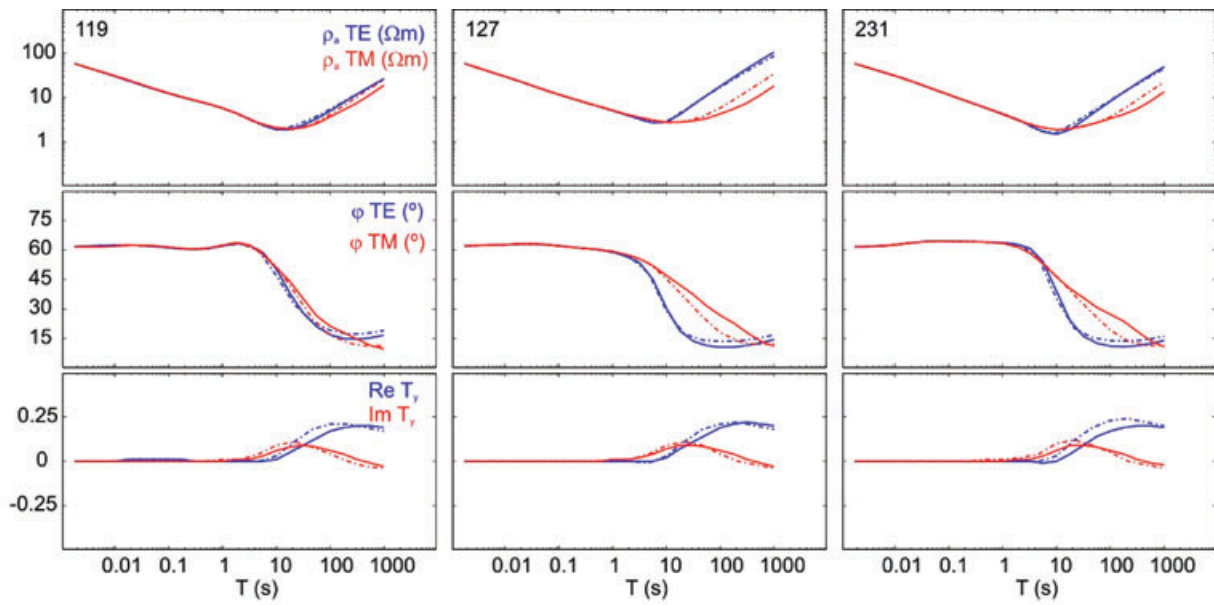
Figure 14. View of the 3-D model used for study of the 3-D effects on the data set. The 3-D model was constructed from a simplified version of the resistivity structures of models from Fig. 9. The horizontal slice shows the resistivity distribution at a depth of 4.2 km. The vertical slice corresponds to the location of profile 1. The inverted triangles mark the (projected) positions of the stations. The upper panel compares the responses of the 3-D model (solid lines) with those of a 2-D model corresponding to a slice of the 3-D model at the location of profile 1 (dashed lines). The inverted red triangles show the location of the stations whose responses are pictured. The relatively small difference between the 2-D and 3-D responses (of the order of the data fit) indicate that the 2-D approach taken is appropriate, although 3-D effects cannot be ruled out altogether.

layers of limestone and sandstone of Cretaceous to Upper Triassic age as revealed by borehole logs. As these materials have significant porosity, they can store significant volumes of fluids, which in turn can lead to increased conductivity. In particular, the borehole cuttings of the geothermal wells at the Groß Schönebeck (Moeck *et al.* 2007) site show alternating sequences of clay-rich formations and weakly consolidated sandstones in the depth of C1 to C4 (between B2 and M1 reflectors in Figs 1 and 8). Regions with the highest conductivity within these shallow layers could correspond to the presence of conductive clay minerals and/or very high porous materials (>15 per cent; Moeck *et al.* 2007) such as unconsolidated sandstones.

As the geometry, depth and conductivity of the deep conductors C5 in profile 1 and C3 in profile 2 is not well resolved, their nature is speculative and subject to different interpretations. Following the smooth inversion models (Fig. 8) the conductors are imaged as extended anomalies reaching depths of 15 km and 10 km, respectively. In this case, they could represent deep-reaching fault systems associated with Variscan collision zones (Joachimstaler fault?). On the other hand, in the tear-zones inversion models, the deep conductors (C2, C5 in profile 1 and C3, C4 in profile 2) appear as more focused anomalies located directly above the basin floor. These conductive bodies coincide with the Rotliegend level and occur below areas where the Zechstein salt layer presents local lows. Below the salt upwelling the conductivity is moderate (5–20 Ωm). The salt lows could be characterized by the presence of anhydrites of Upper Permian age, which are resistant to (or are a remnant of) salt movement. In contrast with a more plastic behaviour of salt, for which smooth upwelling structures are typical, anhydrites show brittle behaviour and are expected to be highly fractured. In this context, the very low bulk resistivities (<1 Ωm) can be explained by virtue of Archie's semi-empirical law (Archie 1942). In its most simple form, it relates bulk resistivity with the resistivity of the pore fluids and the porosity. Assuming fracture-controlled porosity, a formation fluid salinity of 260 g l^{-1} (Giese *et al.* 2001), and a reasonable range of porosities and temperatures (15 per cent and 150°C, respectively according to well logs; Moeck *et al.* 2008) the observed resistivities of 0.1–0.7 Ωm in Fig. 9 can be explained. This interpretation is also supported by the seismic tomography data (Bauer *et al.* 2010) and the statistical join interpretation of both MT and seismic data (Muñoz *et al.* 2010).

CONCLUSIONS

MT data along a main 40-km-long profile centred on the Groß Schönebeck well doublet and a parallel 20-km-long profile located to the east were measured in summer 2006 and winter 2007. Dimensionality and directionality analysis revealed that the data set is compatible with 2-D assumptions, with a dominant geoelectric strike direction of N70°W and N73°W for profiles 1 and 2, respectively.

Two different classes of resistivity models were obtained from regularized inversion, with two different regularization approaches. Classical 2-D smooth inversion (Fig. 8) produces a resistivity cross-section, which resolves a shallow conductive layer (3 km depth) delineating an antiform shape above the Permian evapourites (Zechstein). These models, however, reveal deeper structures (>5 km depth), which do not agree with existing geophysical and geological data. A second class of models is derived using a different regularization approach, the so-called tear-zones inversion. This approach allows dividing the model into several regions in which classical smooth regularization is applied, but without interaction between them. This way strong resistivity contrasts across the tear-zones borders are not penalized. This alternative class of models includes information obtained from seismic tomography (Bauer *et al.* 2010), that is, introducing a high-resistivity basin floor as a constraint in the inversion. With the use of tear-zones inversion the model space can be explored more rigorously and in a target oriented way.

Both model classes produce consistent images of supra-salt structures but they differ in the deeper parts of the models, that is, the presence of a resistive basin floor and the shape and location of deeper conductive anomalies. Sensitivity analysis reveals that the inclusion of deep conductive anomalies (C2 and C5 of profile 1 and C3 and C4 of profile 2) are required to fit the data, but their geometry and resistivity is not uniquely resolved. The two alternative classes of models found with different inversion approaches are equivalent within data accuracy. This equivalence, however, is not inherent to MT, but caused by the data quality. Employing simulation studies we could demonstrate that better constraints on the alternative models would require higher quality data along a more extended profile.

The target-oriented tear-zones inversion (Fig. 9) reveals zones of high conductivity related to areas in the reservoir level (Rotliegend), associated with anhydrite-rich salt lows in the overlaying evapourite layer (Zechstein). In this context, we speculate that the enhanced conductivity is associated with fracturing in the brittle anhydrites, resulting in enhanced hydraulic permeability.

We therefore conclude that MT is an appropriate method for exploration of geothermal reservoirs both in the classic high enthalpy context where clay mineral alterations present resistivity contrast with the background that allows imaging the clay caps located above the reservoirs, as well as in middle to low enthalpy contexts as is the case for Groß Schönebeck. In the latter case, the sensitivity of MT to high-conductivity anomalies can image enhanced permeability areas due to the larger concentration of (possibly) conductive fluids. Additional information on porosity, temperature or fluid salinity is helpful to interpret conductivity anomalies in terms of reservoir properties.

REFERENCES

Archie, G., 1942. The electrical resistivity log as an aid in determining some reservoir characteristics, *Trans. Am. Inst. Miner. Metall. Pet. Eng.,* **146,** 54–62.

Baltrusch, S. & Klarner, S., 1993. Rotliegend-Gräben in NE-Brandenburg, *Zt. Deut. Geol. Ges.,* **144,** 173–186.

Bauer, K., Moeck, I., Norden, B., Schulze, A., Weber, M. & Wirth, A., 2010. Tomographic *P*-wave velocity and vertical velocity gradient structure across the geothermal site Groß Schönebeck (NE German Basin):

relationship to lithology, salt tectonics, and thermal regime, *J. geophys. Res.*, **115,** doi: 10.1029/2009JB006895.

Becken, M. & Burkhardt, H., 2004. An ellipticity criterion in magnetotelluric tensor analysis, *Geophys. J. Int.,* **159,** 69–82.

Buehnemann, J., Henke, C.H., Mueller, C., Krieger, M.H., Zerilli, A. & Strack, K.M., 2002. Bringing complex salt structures into focus – A novel integrated approach, *SEG Expanded Abstracts*, **21,** 446–449.

Egbert, G.D., 1997. Robust multiple-station magnetotelluric data processing, *Geophys. J. Int.,* **130,** 475–496.

Giese, L., Seibt A., Wiersberg T., Zimmer M., Erzinger J., Niedermann S. & Pekdeger A., 2001. Geochemistry of the formation fluids, in: 7. Report der Geothermie Projekte, In situ-Geothermielabor Groß Schönebeck 2000/2001 Bohrarbeiten, Bohrlochmessungen, Hydraulik, Formationsfluide, Tonminerale. GeoForschunsZentrum Potsdam.

Groom, R.W. & Bailey, R., 1989. Decomposition of magnetotelluric impedance tensors in the presence of local three-dimensional galvanic distortion, *J. geophys. Res.,* **94,** 1913–1925.

Hoffmann, N., Jödicke, H. & Horeshschi, L., 2005. Regional distribution of the lower carboniferous culm and carboniferous limestone facies in the North German Basin: derived from magnetotelluric soundings, *Z. Deut. Ges. Geowiss.* **156/2,** 323–339.

Huenges, E., Moeck, I. & the geothermal group of the GFZ, 2007. Directional drilling and stimulation of a deep sedimentary geothermal reservoir, *Sci. Drill.,* **5,** 47–49.

Krings, T., 2007. The influence of robust statistics, remote reference, and a criterion based on horizontal magnetic transfer functions on MT data processing, *Diploma thesis*, WWU Münster – GFZ Potsdam. 108 pp.

Mackie, R.L., Madden, T.R. & Wannamaker, P.E., 2003. Three-dimensional magnetotelluric modeling using difference equations – Theory and comparisons to integral equation solutions, *Geophysics*, **58,** 215–226.

Meju, M., 2002. Geoelectromagnetic exploration for natural resources: models, case studies and challenges, *Surv. Geophys.,* **23,** 133–205.

Moeck, I., Brandt, W. & Schulz, A., 2007. Geological technical final report of the geothermal well GrSk 4/05, unpublished report, Potsdam.

Moeck, I., Schandelmeier, H. & Holl, H.G., 2008. The stress regime in Rotliegend reservoir reservoir of the Northeast German Basin, *Int. J. Earth Sci. (Geol. Rundsch.),* **98(7),** 1643–1657.

Muñoz, G., Bauer, K., Moeck, I., Schulze, A. & Ritter, O., 2010. Exploring the Groß Schönebeck (Germany) geothermal site using a statistical joint interpretation of magnetotelluric and seismic tomography models, *Geothermics,* **39,** 35–45, doi: 10.1016/j.geothermics.2009.12.004.

Pellerin, L., Johnston, J. & Hohmann G., 1996. A numerical evaluation of electromagnetic methods in geothermal exploration, *Geophysics,* **61,** 121–130.

Plein, E., (ed.) 1995. *Norddeutsches Rotliegendbecken, Rotliegend-Monographie Teil II.* pp. 193 eds. Frankfurt a.M., Stratigraphie von Deutschland I., Cour. Forsch.-Inst., Senckenberg.

Popp, T. & Kern, H., 1998, Ultrasonic wave velocities, gas permeability and porosity in natural and granular rock salt, *Phys. Chem. Earth,* **23,** 373–378, doi:10.1016/S0079–1946(98)00040–8.

Ritter, O., Junge, A. & Dawes, G., 1998. New equipment and processing for magnetotelluric remote reference processing, *Geophys. J. Int.,* **132,** 535–548.

Ritter, O., Hoffmann-Rothe, A., Bedrosian, P.A., Weckmann, U. & Haak, V, 2005. Electrical conductivity images of active and fossil fault zones, in: *High Strain Zones: Structure and Physical Properties,* pp. 165–186 eds. Bruhn, D. and Burlini, L. The Geological Society, London.

Rodi, W. & Mackie, R.L., 2001. Nonlinear conjugate gradients algorithm for 2-D magnetotelluric inversions, *Geophysics,* **66,** 174–187.

Tikhonov, A.N. & Arsenin, V.Y., 1977. *Methods for Solving Ill-Posed Problems,* Nauka, Moscow.

Weckmann, U., Magunia, A. & Ritter, O., 2005. Effective noise separation for magnetotelluric single site data processing using a frequency domain selection scheme, *Geophys. J. Int.,* **161,** 456–468.

Weckmann, U., Ritter, O., Jung, A., Branch, T. & de Wit, M., 2007. Magnetotelluric measurements across the Beatie magnetic anomaly and the Southern Cape Conductive Belt, South Africa, *J. geophys. Res.,* **112,** B05416, doi: 10.1029/2005JB003975.

Wright, P., Ward, S., Ross, H. & West, R., 1985. State-of-the-art geophysical exploration for geothermal resources, *Geophysics,* **50,** 2666–2699.

Ziegler, P.A., 1990, *Geological Atlas of Western and Central Europe : Shell International Petroleum Maatschappij B.V,* 2nd edn pp. 239 Geological Society of London, Elsevier, Amsterdam.